ScintPi measurements of low-latitude ionospheric irregularity drifts using the spaced-receiver technique and SBAS signals

Josemaria Gomez Socola[1], Fabiano S. Rodrigues[1], Isaac G. Wright[1], Igo Paulino[2] and Ricardo Buriti[2]

[1]W.B. Hanson Center for Space Sciences, The University of Texas at Dallas, Dallas, 75080, United States
[2]Department of Physics, Federal University of Campina Grande, Campina Grande, 58429-900, Brazil

Correspondence to: Josemaria Gomez Socola (Josemaria.GomezSocola@utdallas.edu)

Abstract. Previous efforts have used pairs of closely-spaced specialized receivers to measure Global Navigation Satellite System (GNSS) signals and to estimate ionospheric irregularity drifts. The relatively high cost associated with commercial GNSS-based ionospheric receivers limited somewhat their deployment and the estimation of ionospheric drifts. The development of an alternative low-cost GNSS-based scintillation monitor (ScintPi) motivated us to investigate the possibility of using it to overcome this limitation. ScintPi monitors can observe signals from geostationary satellites, which can greatly simplify the estimation of the drifts. We present results of an experiment to evaluate the use of ScintPi 3.0 to estimate ionospheric irregularity drifts. The experiment consisted of two ScintPi 3.0 deployed in Campina Grande, Brazil (7.213°S, 35.907°W, dip latitude ~14°S). The monitors were spaced by 140 m in the magnetic east-west direction and targeted the estimation of the zonal drifts associated with scintillation-causing equatorial spread F (ESF) irregularities. Routine observations throughout an entire ESF season (September 2022 – April 2023) were made as part of the experiment. We focused on results of irregularity drifts derived from geostationary satellite signals. The results show that the local time variation in the estimated irregularity zonal drifts is in good agreement with previous measurements and with the expected behavior of the background zonal plasma drifts. Our results also reveal a seasonal trend in the irregularity zonal drifts. The trend follows the seasonal behavior of the zonal component of the thermospheric neutral winds as predicted by the Horizontal Wind Model (HMW14). This is explained by the fact that low latitude ionospheric F-region plasma drifts are controlled, in great part, by Pedersen conductivity weighted flux tube integrated zonal neutral winds. The results confirm that ScintPi has the potential to contribute to new, cost-effective measurements of ionospheric irregularity drifts in addition to scintillation and total electron content. Furthermore, the results indicate that these new ScintPi measurements can provide insight on ionosphere-thermosphere coupling

1 Introduction

A series of low-cost, easy to install and easy to maintain ionospheric scintillation and total electron content (TEC) monitors were developed at UT Dallas (e.g., Rodrigues and Moraes, 2019; Gomez Socola and Rodrigues, 2022). These monitors are referred to as ScintPi and were developed using commercial off-the-shelf (COTS) Global Navigation Satellite System (GNSS) receivers and single-board computers (Raspberry Pi). While ScintPi monitors were not developed to fully replace commercial monitors, they can be used in various scientific and educational applications. For instance, ScintPi monitors have been successfully used in studies of low and low-to-mid latitude ionospheric irregularities and TEC depletions (e.g., Sousasantos et al., 2023,2024; Gomez Socola et al., 2023), in studies of solar radio bursts and their impact on GNSS signals (Wright et al., 2023a) and in student projects related to space weather (Wright et al., 2023b).

Given that ScintPi has a reduced sampling rate (20 Hz) and C/No resolution (1 dB-Hz) compared to typical commercial scintillation monitors, the ability of ScintPi to produce satisfactory drift estimates needed to be investigated. On the other hand, ScintPi is capable of monitoring signals transmitted by geostationary satellites, which would greatly simplify the analyses associated with and interpretation of irregularity drift measurements.

Therefore, here we present results of an experimental effort to evaluate the use of ScintPi monitors to estimate ionospheric irregularity drifts. The approach follows that of the so-called closely-spaced scintillation technique which measures time differences between the occurrence of scintillation patterns observed by closely-spaced receivers to infer the horizontal velocity component of scintillation-causing irregularities along the receivers baseline.

Ionospheric plasma drifts represent an important feature of the ionospheric plasma behavior and are responsible for controlling plasma transport and structuring. For instance, vertical (upward) F-region plasma drifts drive the transport of plasma from the magnetic equator to low latitudes through the ionospheric plasma fountain effect (Hanson and Moffett, 1966; Moffett, 1979). This mechanism gives rise to the Equatorial Ionization Anomaly – EIA (Appleton, 1946; Bailey 1948). Additionally, the so-called pre-reversal enhancements (PRE) in vertical drifts, occurring near sunset, is known to control the development of equatorial spread F – ESF (Heelis et al., 1974; Farley et al., 1986; Fejer et al., 1999; Fesen et al., 2000).

The magnetic zonal component of the F-region plasma velocity at low latitudes, on the other hand, can reflect the level of coupling between the upper thermosphere and ionosphere (Immel et al., 2006; Wang et al., 2021). During nighttime, the E-region dynamo is greatly reduced, and F-region plasma drifts should reflect the effects of the F-region dynamo alone (e.g., Coley et al., 1994).

60 Ionospheric plasma drifts are also relevant in certain applications. According to Carrano and Groves, (2010), the probability of experiencing loss of lock and likelihood of extended signal reacquisition times depend on factors such as the velocity of the satellite motion with respect to the geomagnetic field and plasma drifts.

Obtaining ground-based measurements of background ionospheric plasma drifts presents significant challenges. For instance,
65 the incoherent scatter radar (ISR) of the Jicamarca Radio Observatory (JRO) is the only instrument capable of making observations of vertical and zonal plasma drifts. While the measurements can be conducted across various heights within the F-region, the observations require the operation of high-power transmitters which limit the number of measurements per year.

The motion of ionospheric irregularities can be measured more easily than the motion of the background ionospheric plasma
70 using, for instance, L-band spaced scintillation receivers.(Kil et al., 2000,2002; Ledvina et al., 2004; Kintner et al., 2004; Kintner and Ledvina, 2005; Cerruti et al., 2006; Otsuka et al., 2006; Sobral et al., 2009; de Paula et al., 2010; Muella et al., 2008,2009,2012,2014,2017; Cesaroni et al., 2021). Irregularity drifts are often used as an indicator of background plasma drifts at low latitudes. The application of the scintillation-based spaced receiver technique to measure irregularity drifts is revisited in this study with focus on using more cost-effective instrumentation for the measurements.
75

Gomez Socola and Rodrigues (2022) already addressed the ability of the sampling rate (20 Hz) and amplitude resolution (1 dB-Hz) of ScintPi 3.0 measurements to produce amplitude scintillation indices that are comparable to those produced by commercial GNSS-based monitors. Here, we present results of an experimental setup and campaign that targeted evaluating the ability of applying the scintillation-based spaced receiver technique to ScintPi 3.0 measurements and estimate irregularity
80 drifts.

The presentation of our work is organized as follows: In Sect. 2 we provide information about the ScintPi 3.0, measurements, spaced-receiver experimental setup and geophysical conditions under which measurements were made. Sect. 3 describes the methodology used to derive irregularity drifts from the ScintPi measurements. In Sect. 4 we present and discuss the results of
85 the measurements and analyses. Sect. 5 summarizes our main findings.

2 Experimental setup

Scintillation observations were carried out using ScintPi 3.0 monitors. ScintPi 3.0 can be described as a multi GNSS constellation, dual-frequency ionospheric scintillation and total electron content (TEC) monitor. ScintPi was developed at UT Dallas using a COTS GNSS receiver and a single-board computer (Raspberry Pi).
90

The development of ScintPi was motivated by the relatively high cost of commercial GNSS-based scintillation and TEC monitors. While it is not intended to fully replace commercial monitors, ScintPi allows different research and educational initiatives. Details about ScintPi 3.0, along with illustrative examples of measurements and comparison with collocated observations made by commercial receivers are described in Gomez Socola and Rodrigues (2022). Examples of different types of studies using ScintPi measurements can be found in Gomez Socola et al. (2023), Sousasantos et al. (2023; 2024) and Wright et al. (2023a). Results of an educational effort using ScintPi can be found in Wright et al. (2023b). Of relevance to this study is that ScintPi can measure the strength of signals transmitted by GNSS satellites, achieving sampling rates of 20 Hz and C/No resolution of 1 dB-Hz. In this study, our focus centers on the analysis of signals transmitted by geostationary satellites. The use of geostationary satellites simplifies the analyses and the interpretation of the measurements.

2.1 Deployment and spacing

Because low-latitude equatorial plasma bubbles (EPBs) and ionospheric irregularities associated with them are known to move in the magnetic zonal direction (Dyson and Benson, 1978; Mendillo and Baumgardner, 1982; Martinis et al., 2003, 2020), the two monitors were placed along the east-west magnetic direction spaced by 140 m. The site is in a region of -21.39° magnetic declination based on magnetic values from the International Geomagnetic Reference Field - IGRF-13 (Alken et al., 2021) (See Fig. 1b). The spacing was chosen based on expected values of low latitude irregularity drifts, sampling rate of the receivers, and availability of locations. The sampling rate of the receivers (or sampling frequency, f_s), the spacing between receivers (d), and the apparent component of the irregularity velocity along the baseline (v'_{scint}) dictate the delay (in samples, $N \sim f_s d / v'_{scint}$) between the two patterns observed by the spaced receivers. Additional details will be provided in Section 3. Figure 1a shows the location of the observation site (UFCG). Figure 1b and 1c describe the placement of the receivers.
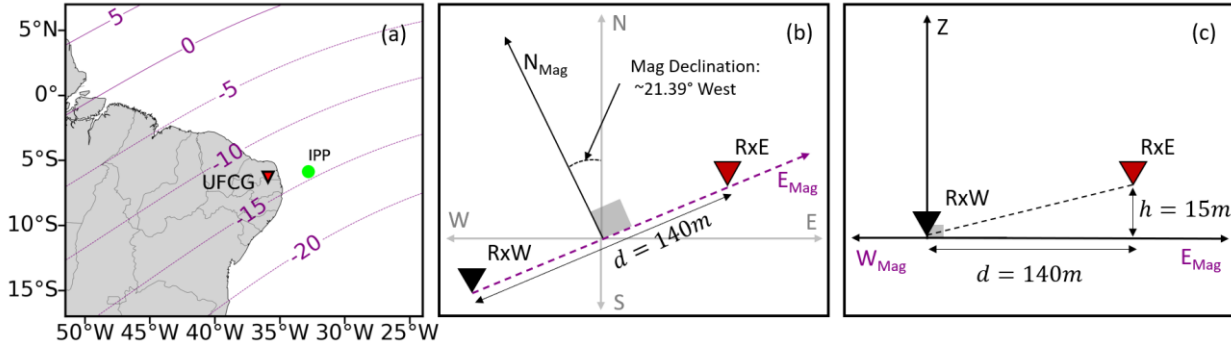
Figure 1: (a) Map showing the location of UFCG where spaced ScintPi 3.0 monitors have been deployed for this study. UFCG is located at ~14° dip latitude where L-Band scintillations occur frequently. Panels (b) and (c) are diagrams showing the placement of the monitors along the magnetic zonal direction for estimation of ionospheric irregularity drifts using the scintillation-based spaced-received technique

2.2 Measurements

While ScintPi 3.0 can make measurements of signals transmitted by different GNSS satellites (GPS, GLONASS, Beidou, and Galileo), in this study we focused on measurements of signals transmitted by geostationary satellites which can also be measured by ScintPi 3.0. The use of geostationary signals has various advantages. For instance, signals from geostationary satellites provide observations over a fixed location allowing for unambiguous interpretation of the variability in the observed drifts. Additionally, the decorrelation times of the observed signal fluctuations are not affected by satellite velocities. Perhaps more importantly, the satellite velocity does not have to be considered in the analyses and calculations of ionospheric irregularity drifts.

The signals recorded by GNSS receivers are coded using pseudo-random noise (PRN) sequences, which are codes that each satellite transmits to differentiate itself from other satellites. At the location of UFCG, ScintPi 3.0 monitors can decode signals from the Astra-5B (PRN123) and Astra Ses-5 (PRN136) geostationary satellites, stationed at 31.5°E and 5°E geographic longitudes, respectively. Unfortunately, data from PRN123 had to be excluded due to its low elevation angle (~14°) which led to non-geophysical amplitude fading caused by multipath. PRN136, on the other hand, was positioned at an elevation angle of 42° and azimuth of 84° which provided adequate measurements for this study. The ionospheric pierce point (IPP) for the PRN136 signal is located at 6.77°S, 31.86°W (dip latitude ~15°S), as shown in Fig. 1a. The IPP calculation followed the method outlined by Prol et al. (2017), considering the altitude of the ionospheric F-region peak density at 450 km.

For this study, we analyzed 8 months (September 1, 2022 – April 30, 2023) of nearly continuous measurements. The measurements covered an entire ESF season in Brazil when scintillations occur frequently. The measurements were made during the ascending phase of solar cycle 25, and the mean solar flux for the period was 148.23 SFU.

3 Scintillation pattern velocities and ionospheric irregularity drifts

As previously mentioned, ScintPi 3.0 measures the strength of L-band signals transmitted by geostationary satellites. These signals are subject to diffraction by irregularities in the ionospheric plasma density, giving rise to intensity fading (scintillation) patterns observed by monitors on the ground.

At low magnetic latitudes, ionospheric irregularities are known to be elongated along the magnetic field lines and to drift in the zonal magnetic direction (Dyson and Benson, 1978; Mendillo and Baumgardner, 1982; Martinis et al., 2003, 2020). Therefore, an approach to estimate zonal irregularity drift is to measure the scintillation pattern velocity using receivers that are spaced in the magnetic zonal direction.

An experimental setup commonly used to measure the scintillation pattern velocity relies on the estimation of the time delay between scintillation patterns observed by spaced scintillation receivers. This time delay is quantified by the time lag at which the cross-correlation function of the measured signals reaches its maximum (τ_0). The measured (or apparent) scintillation velocity along the receiver baseline (v'_{scint}) is then quantified from $v'_{scint} = d/\tau_0$, where d represents the spacing between the receivers (Kil et al., 2000).

In this study, we take into consideration the approach introduced by Briggs et al. (1950) which compensates for the temporal evolution of the intensity pattern. This approach is known as the "full correlation method" and has been widely used in estimation of irregularity drifts (e.g., Kil et al., 2000; Kintner et al., 2004; Kintner and Ledvina, 2005; Otsuka et al., 2006; Sobral et al., 2009; de Paula et al., 2010; Muella et al., 2008,2009,2012,2014,2017). We summarize the approach in the following paragraphs.

Briggs et al. (1950) pointed out that the apparent velocity (v'_{scint}) has contribution from the random-like evolution of scintillation-causing irregularities as they move between the line-of-sight of the two observing receivers. The apparent velocity can be related to the true velocity (v_{scint}) through the following expression (Briggs et al.,1950):

$$v_{scint} = \frac{v'_{scint}}{1+t_0^2/\tau_0^2}, \tag{1}$$

Where t_0 is the so-called characteristic time and is the time at which the autocorrelation of the scintillation pattern matches the maximum cross-correlation value. This time is associated with a random component in the motion of the plasma density irregularities and, therefore, the ratio t_0^2/τ_0^2 determines the extent to which the apparent and the true velocity are equivalent. For instance, when random motion (decorrelation) is negligible, the cross-correlation value for the two scintillation patterns approaches 1. As a result, t_0 will approach 0 and the ratio t_0^2/τ_0^2 will be negligible. The measured velocity would then match the true velocity ($v_{scint} \sim v'_{scint}$). In contrast, situations where t_0 and t_0^2/τ_0^2 depart from 0 indicate that the scintillation pattern velocity has non-negligible contributions from random motion (Kintner et al., 2004). Finally, to quantify the contribution from random motions to the observed velocities, Briggs et al. (1950) introduced the so-called characteristic velocity (v_c):

$$v_c = v_{scint}\left(\frac{t_0}{\tau_0}\right) = \frac{v'_{scint}}{1+t_0^2/\tau_0^2}\left(\frac{t_0}{\tau_0}\right), \tag{2}$$

Combining Eq. (1) and Eq. (2) one can write:

$$v'_{scint} = v_{scint} + \frac{v_c^2}{v_{scint}}, \tag{3}$$

Equation 3 shows, more explicitly, that the measured pattern velocity (v'_{scint}) has contributions from the true irregularity drifts and from the random characteristic irregularity velocity.

Figure 2 illustrates the estimation of τ_0 and t_0 used to compute true velocities (Eq. 1) and characteristic velocities (Eq. 2). Figure 2a shows a 60-second interval of signal strengths measured by the receivers at UFCG. Note that, despite the low C/No resolution (1 dB-Hz), similar fluctuations are observed by both receivers. Also note that fluctuations observed by the west receiver (RxW) precede the fluctuations observed by the east receiver (RxE) indicating eastward motion. Figure 2b shows the cross-correlation function between these two signals. From the maximum cross-correlation coefficient we obtain the time delay (τ_0) needed to compute the apparent pattern velocity (v'_{scint}). Figure 2c shows the autocorrelation of the scintillation pattern measured by the west receiver. The maximum cross-correlation coefficient is used to estimate the characteristic time (t_0) (see gray line in panels b and c). Again, we point out that, for high cross-correlation values (say correlation coefficient ~ 1), t_0 and t_0^2/τ_0^2 would have negligible values, and the apparent velocity (v'_{scint}), Eq. (1) would converge to the true irregularity velocity (v_{scint}).
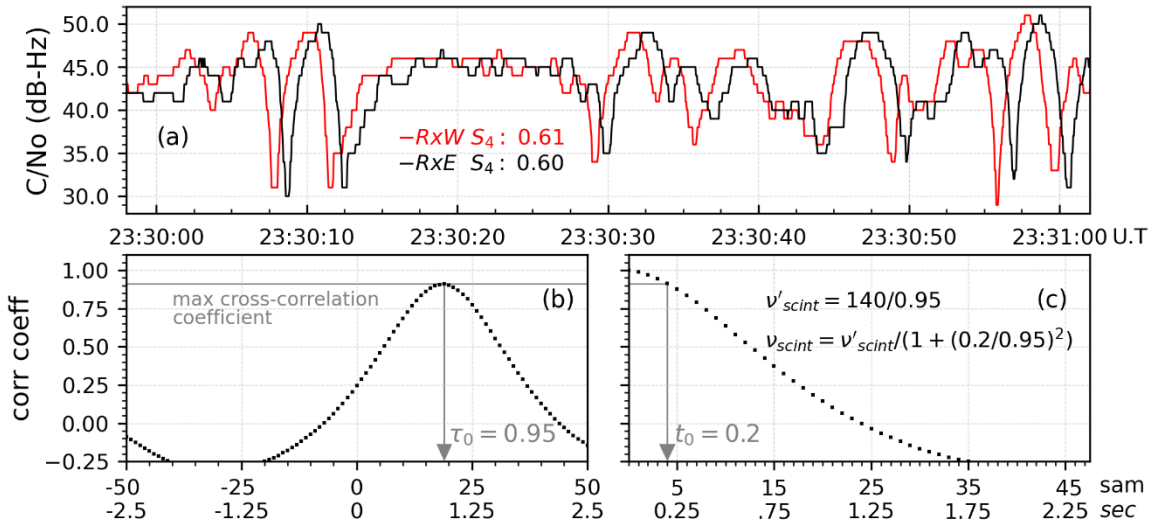
Figure 2 – Illustration of calculation used to derive the characteristic time (t_0) and the time lag of maximum correlation (τ_0). Panel (a) shows an example of 60-second signal strength measurements made with closely spaced ScintPi 3.0 monitors on October 4, 2022. Panel (b) shows the cross-correlation function between power series from the two receivers, and panel (c) shows the autocorrelation for the west receiver. The maximum cross-correlation coefficient is used to estimate the characteristic time associated with the signal decorrelation. The horizontal axis in panels (b) and (c) show both sample number (samp) and time in seconds.

3.1 Further considerations

While most studies (e.g., Kil et al., 2000; Otsuka et al., 2006; de Paula et al., 2010) have used the Brigg's formulation (Eq. 1), Ledvina et al. (2004) presented further analysis of the spaced-receiver technique and pointed out additional considerations. First, they pointed out the fact that the scintillation pattern velocity is a projected representation of the velocity of the irregularities, and this velocity will depend, in general, on geometric factors involving the placement of the receivers and the Earth's magnetic field. For instance, differences in the altitudes of the two receivers should be taken into consideration in the estimation of the drifts. They showed that Eq. (1) can be updated to take into consideration differences in the heights of the receivers (Ledvina et al., 2004):

$$v_{scintx} = \left[1 - \frac{\Delta h}{d}\tan(\theta_{vz})\right]\left[\frac{v'_{scintx}}{1+t_0^2/\tau_0^2}\right], \tag{4}$$

200

Where v_{scintx} represents the scintillation pattern velocity in the east-west direction parallel to the Earth's surface, d is the zonal spacing of the receivers, Δh is the height difference of the receivers, and θ_{vz} is a projection angle in the vertical-zonal plane. The projection angle is given by (Ledvina et al., 2004):

$$\theta_{vz} = \tan^{-1}\left[\frac{\tan(\phi)\sin(\theta)-(B_x/B_y)\tan(\phi)\cos(\theta)}{1-(B_z/B_y)\tan(\phi)\cos(\theta)}\right], \tag{5}$$

205   Where ϕ is the satellite zenith angle and θ is the satellite azimuth angle relative to the magnetic meridian (magnetic north). B_x, B_y, and B_z are components of geomagnetic field vector at the IPP location in the magnetic east, north and vertical directions, respectively. B_x is close to zero and the second term in the tan^{-1} argument is negligible. The IPP was computed using a mean ionospheric altitude of 450 km that is thought to be adequate for the location and solar flux conditions of the observations (e.g., Nava et al., 2007). Perhaps more importantly, different choices of ionospheric altitude (say, 300 to 600 km)
210   produce similar values of geomagnetic components and do not affect our drift estimates and results.

Using long-term averages of the GNSS coordinates provided by the receivers we found a height difference of ~15 meters (Fig. 1c). Taking into consideration values for the experiment at UFCG (described in Section 2.2), the expression for the irregularity drifts using the geostationary measurements is updated to:

215    $$v_{scintx} = \left(1 - \frac{15.3}{140}\left[\frac{\tan(48)\sin(84-(-21.39))}{1-\left(\frac{B_z}{B_y}\right)\tan(48)\cos(84-(-21.39))}\right]\right)\left[\frac{v'_{scintx}}{1+t_0^2/\tau_0^2}\right] = (0.899)\left[\frac{v'_{scintx}}{1+t_0^2/\tau_0^2}\right], \tag{6}$$

Ledvina et al. (2004) also pointed out that deriving zonal irregularities drifts from the scintillation pattern velocity can be affected by vertical ionospheric drifts (v_{iz}) at the IPP location. The vertical drifts would affect the scintillation pattern velocity as follows:

$$v_{scintx} = v_{zonal} + \left[\frac{-\tan(\phi)\sin(\theta)}{1-(B_z/B_y)\tan(\phi)\cos(\theta)}\right]v_{iz}, \tag{7}$$

220   Where (B_z/B_y) is equivalent to the tangent of inclination angle of the geomagnetic field ($-(\tan(\vartheta_{dip}))$) at the IPP location, and v_{iz} is the vertical irregularity drift.

For our experimental setup, $\phi = 48°$, $\theta = (105.39°)$, and ϑ_{dip} = -29.62° resulting in $v_{scintx} = v_{zonal} - 0.917\,v_{iz}$. Where, the azimuth refers to the geographic azimuth of the satellite relative to the magnetic meridian. This means that, for our experimental
225   configuration, the vertical drifts in conjunction with the geometry of the signal path can contribute to the magnitude of the observed scintillation pattern velocities. Outside the pre-reversal enhancement (PRE) time that occurs around sunset, vertical

drifts are expected to be much smaller than the values of zonal drifts. Following previous studies (e.g., Cesaroni et al., 2021), the effect of the vertical drifts is not corrected in our analyses.

4 Results and discussion

230 **4.1 On the estimation of irregularity drifts velocities**

We now present and discuss the measurements made by the UFCG ScintPi monitors and the zonal irregularity drifts derived from these measurements. Figure 3 shows a representative example of the measurements and results. The measurements are for the night between October 4 and 5, 2022.

235 Figure 3a shows L1 C/No values for the PRN136 signal measured by the two receivers. It shows that, as expected, similar variations in scintillation occurrence and magnitude were observed in both signals. Figure 3b shows 1-minute S4 index values computed for both signals. The S4 index is a widely index used in scintillation studies to quantify amplitude scintillation (Groves et al., 1997; Kil et al., 2002; Nishioka et al., 2011) and can be defined as the standard deviation of the signal intensity normalized by its average. The observed S4 values indicate (i) strong L-Band scintillation occurring from 22:30 to 23:45 UT
240 (20:30 to 21:45 LT) and (ii) moderate to weak scintillation between 00:30 and 02:30 UT (22:30 to 00:30 LT). Note that the estimates of S4 for both signals provide nearly identical values most of the time, which indicates similar variability in the intensity patterns. This similarity in the signals is better quantified in the high cross-correlation coefficients (i.e., $|r| \geq 0.75$) presented in Fig. 3c.

245 Figure 3c also shows that, despite the reduced resolution of the signal intensities, high correlation values can still be derived from ScintPi measurements. Additionally, we point out that high cross-correlation coefficients persisted even during weak scintillation activity (i.e., S4 in the 0.2 - 0.4 range), indicating that one can compute irregularity drifts even during periods of weak L-Band scintillation.

250 Figure 3d presents the estimates of the characteristic velocity (v_c). The characteristic velocity has been averaged in 3-minute bins (average of 3 values). The error bars represent the standard deviation of the values used in the averages. One can observe that characteristic velocity shows higher values early in the evening. We attribute this to periods of more turbulent irregularity motion associated with the development of EPBs. This turbulent or random behavior has been observed in previous studies (e.g., Spatz et al.,1988; Bhattacharyya et al, 2001; Valladares et al., 2002; Kintner et al.,2004; Otsuka et al., 2006).
255

Finally, Fig. 3e shows our estimates (3-min averages) of the corrected true scintillation pattern velocities (v_{scintx}). Again, error bars represent the standard deviation of the values used in the averages. As expected, the scintillation pattern velocities

reveal a behavior that is similar to that expected for the low latitude drifts. They show strong eastward drifts early in the evening with weakening drifts towards midnight.
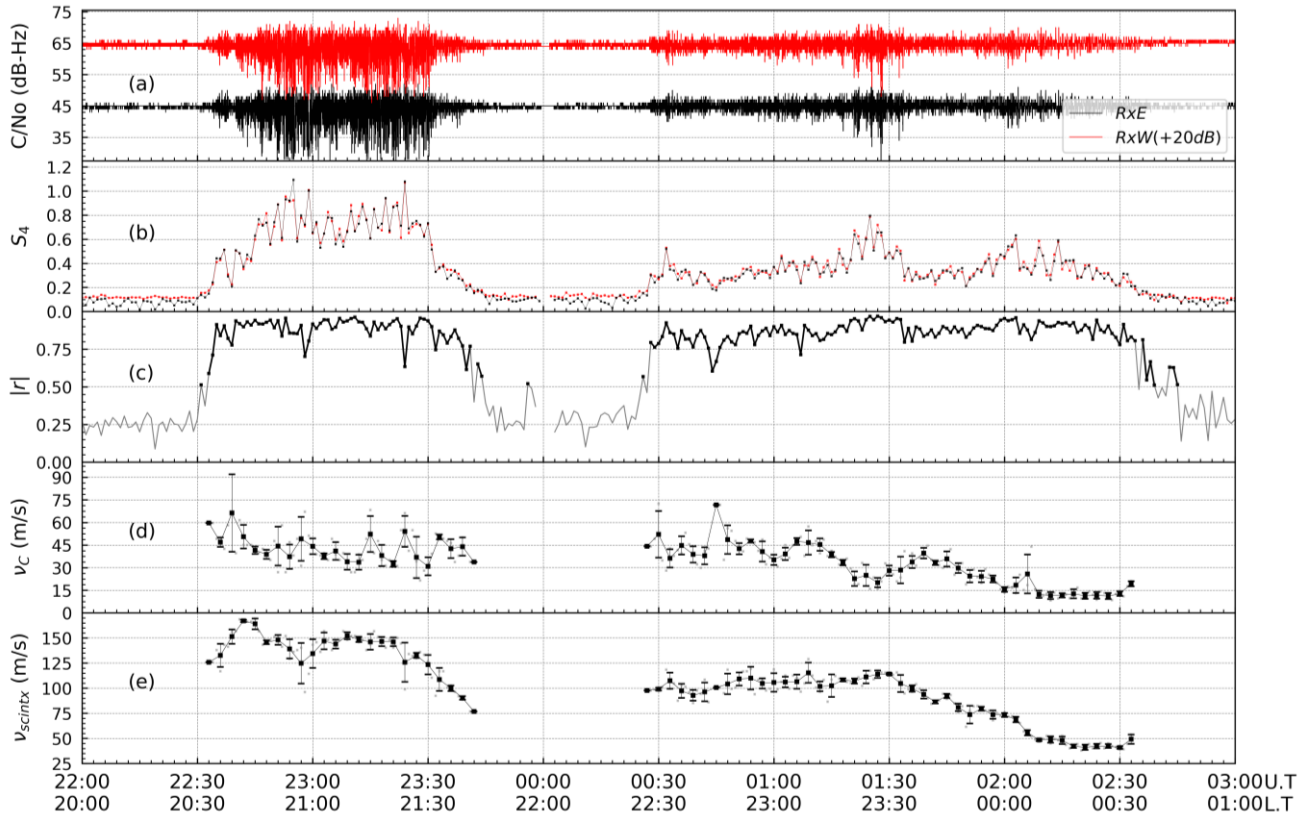
Figure 3 - Example of measurements and analyses made with closely spaced ScintPi 3.0 monitors at UFCG for the same night of Fig. 2 (October 4-5, 2022). (a) Signal strenghts (C/No) in dB-Hz from L1 from PRN136. (b) Severity of scintillation, i.e., S4 index. (c) Maximum value of the normalized cross correlation function |r|. Only pattens for which |r| > 0.5 (highlighted) are used in the computation of the scintillation pattern velocity in this study. (d) Estimated mean characteristic velocities, (e) Estimated mean true scintillation pattern velocities. Error bars in panels (d) and (e) represent standard deviation around the mean of the values used in 3-minute bins.

4.2 On the seasonal variability of zonal irregularity drifts

The analysis described in Sect. 4.1 was applied to a data set containing 242 observation nights between September 1, 2022 and April 30, 2023. The period covers the equatorial spread F (ESF) season in Brazil (Abdu et al., 2003) when scintillation is observed. This period also has measurements from two equinoxes and December solstice. The results are summarized in Fig. 4.

Figure 4a shows the variation of the observed L-Band (1.575 GHz) scintillation as a function of local time and day of the campaign. The vertical white lines indicate missing data because of power outages at least one of the receiver sites. Figure 4a also shows the day-to-day variability of scintillation activity observed by the monitors. It also shows that scintillation occurred in most days. Figure 4a shows that L-Band scintillation was observed, mostly, between 20:00 LT and local midnight. During some days, however, scintillation occurred until 02:00 LT.

Figure 4b summarizes the magnetic zonal irregularity drift results. The drifts show a behavior that indeed is similar to what would be expected for background nighttime ionospheric plasma drifts at low latitudes (Fejer et al., 1991; Fejer et al., 2005). The drifts are predominantly eastward, with larger values (120 – 200 m/s) in the beginning of the evening, gradually decreasing to 20-80 m/s by midnight and into the post-midnight sector. The results in Figure 4c also show a trend, with lower drift values in September/October and April/May and higher values in the months between.

As mentioned earlier, zonal irregularity drifts are often assumed to be tracers of ionospheric plasma drifts (Ledvina et al., 2004). At low latitudes, theoretical analysis suggest that nighttime zonal drifts are expected to be controlled, in most part, by zonal F-region winds (Rishbeth et al., 1972; Heelis et al., 1974). For instance, zonal plasma drifts are related to zonal neutral winds (Uz) through a flux-tube integrated Pedersen conductivity weighted integral which is representative of the neutral wind dynamo (Haerendel et al., 1992):

$$v_{zonal} \sim \frac{1}{\Sigma_P} \int \sigma_p U_z \mathrm{ds} \tag{8}$$

Where the integral is performed along a magnetic field line, σ_p is the Pedersen conductivity and Σ_P is the Pedersen conductance. At night, E-region conductivities are greatly reduced and zonal drifts are expected to have contributions coming, predominantly, from winds at F-region heights.

Figure 4c shows the magnetic zonal component of the neutral winds at F-region heights (450 km) over UFCG predicted by the Horizontal Wind Model 14 (HWM14). HWM14 is an empirical model of the neutral winds developed using an extensive set of measurements (Drob et al., 2015). It provides estimates of the geomagnetically quiet time behavior of the thermospheric winds. Similar to the observed behavior of the irregularity drifts, Figure 4c shows stronger eastward winds in the beginning of the evening and weaker winds towards midnight and into the post-midnight sector. Additionally, HWM14 results show weaker zonal winds in September/October and April/May, contrasting with stronger zonal winds in the months between November and March. The similarity in the behavior between drifts and winds is impressive, given that the plasma drifts depend on combined contributions of winds along magnetic fields, weighted by the conductivity values. We must point out that similarities in the behavior of EPB and neutral wind magnetic zonal velocities have been reported out before using, for instance, same-night observations made by airglow cameras and Fabry-Perot Interferometers (FPI) located near our site (UFCG) in Brazil (Chapagain et al., 2012).
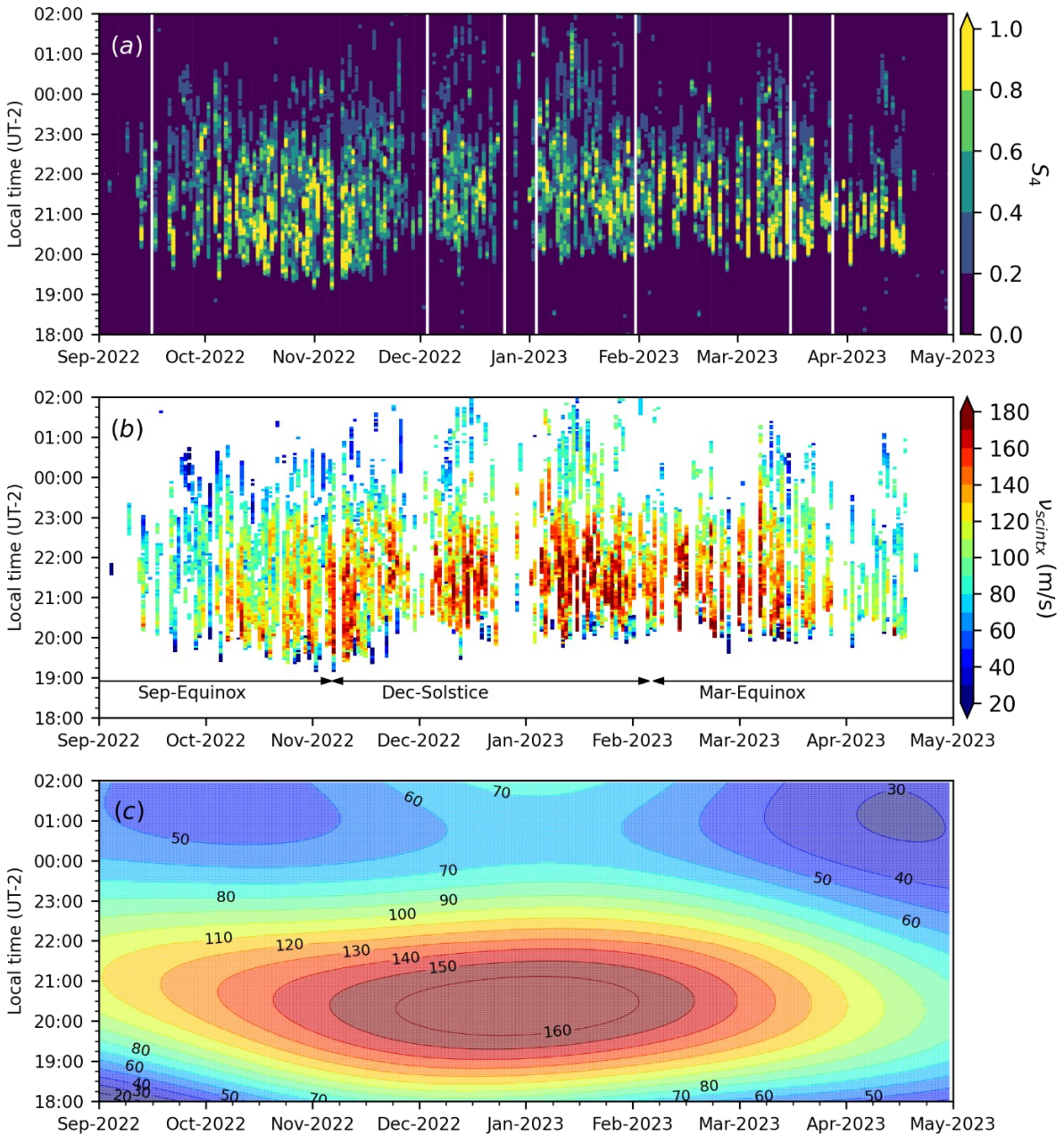
Figure 4 - Panel (a) shows the average S4 index measurements as a function of local time (LT = UT − 2) and date for 242 nights between September 1, 2022, and April 30, 2023. The average is for the two S4 values computed by the spaced monitors. White lines indicate lack of data caused by power outages at the observation sites. Panel (b) shows zonal irregularity drifts. Different seasons determined as +/- 45 days around equinox and solstice days are also indicated. Panel (c) shows climatological zonal wind velocities (Uz) from the Horizontal Wind Model 14 (HWM14) for a height of 450 km over UFCG, its values magnitude values are indicated by labels of the contour lines.

We point out that the magnitudes of the winds and irregularity drifts differ, with irregularity drifts being, in general, larger than the zonal winds. The difference is attributed to the fact the drifts are the result of conductivity weighted winds along the magnetic field lines (Eq. 5) and the HWM14 winds shown here are for a single height and location (450 km above UFCG).
315 Observations of neutral winds larger than ionospheric drifts have been reported in previous studies (e.g., Wharton et al., 1984; Coley et al., 1994; Navarro and Fejer, 2020). Additionally, HWM14 does not have a solar flux dependency and are representative of the solar conditions under which the drift measurements were made.

Finally, we also point out cases of very low irregularity drift values early in the evening on certain observation nights. See, for
320 instance, blue markers in some of the drift measurements between 19:00 and 20:30 LT in Fig. 4b. We hypothesize that these low values of zonal drifts can be caused by the contribution of large vertical drifts, associated with the PRE, to the estimates of zonal drifts (Eq. 7). Estimates of nighttime vertical drifts derived from digisonde data for a low-latitude site in Brazil have revealed cases of upward drifts as large as 40 m/s during the same timeframe of 19:00 and 20:30 LT (e.g. Abdu et al., 2006).

5 Conclusions

325 We presented results of an experiment to evaluate the use of ScintPi 3.0 to estimate ionospheric irregularity drifts. ScintPi 3.0 is an alternative, low-cost GNSS-based scintillation monitor developed to enable research, education, and citizen science initiatives (Gomez Socola and Rodrigues, 2022). Of relevance to this study is that ScintPi 3.0 is capable of measuring signals transmitted by geostationary satellites.

330 The experiment used the spaced-receiver scintillation technique for measurements of ionospheric irregularity drifts (Briggs et al., 1950; Ledvina et al, 2004). It also used measurements made by two ScintPi 3.0 deployed in Campina Grande, Brazil (7.21°S, 35.91°W, dip latitude ~14°S). The monitors were spaced by 140 m in the magnetic east-west direction to measure the zonal component of the drifts associated with scintillation-causing equatorial spread F (ESF) irregularities.

335 We analyzed measurements made throughout an entire ESF season, between September 2022 and April 2023. We focused our analyses on irregularity drifts derived from geostationary satellite signals, which simplify the analyses and interpretation of the results.

The results confirm that ScintPi 3.0, despite its low cost and low C/No resolution (1 dB-Hz), can measure irregularity drifts.
340 The cross-correlation of the signals is mostly well above 0.75 even during late-night weak scintillation. Our drift calculation results also show that the local time variation in the estimated irregularity zonal drifts is in good agreement with previous experimental studies and with theoretical expectations for the behavior of the low-latitude background zonal plasma drifts (e.g.,

Haerendel et al., 1992; Fejer et al., 2005; Shidler and Rodrigues, 2021). The drifts are predominantly eastward, with largest values early in the evening and weakening drifts towards local midnight.

345

Our results also reveal a seasonal trend in the irregularity zonal drifts. We found that this trend is well correlated with the behavior of the zonal component of the thermospheric neutral winds as predicted by the Horizontal Wind Model (HMW14). The similarity between the behavior of the neutral winds and observed irregularity drifts is a manifestation of the F-region dynamo, which controls the zonal F-region drifts at night (e.g., Haerendel et al., 1992).

Data availability

350

The ionospheric irregularity drift dataset is publicly available at Zenodo via https://zenodo.org/records/14289996. [Gomez Socola, J., 2024]

Author contribution

JGS and FSR proposed the experiment and IP and RB host it at UFCG. JGS and IP oversaw the acquisition of data during the
355 campaign. JGS performed the analyses with contributions from IW. JGS and FSR interpreted the results and prepared the manuscript with contributions from all co-authors.

Competing interests

The authors declare that they have no conflict of interest.

Acknowledgements

360 Work at UTD was supported by the National Science Foundation (NSF) Award AGS-2122639 and by the NSF's GRFP Grant No. 2136516. I. Paulino would like to thank Conselho Nacional de Desenvolvimento Científico e Tecnológico (CNPq) for supporting this research under contract 309981/2023-9.

References

Abdu M.A., Batista I.S., Reinisch B.W., Sobral J.H.A., Carrasco A.J. Equatorial F region evening vertical drift, and peak
365 height, during southern winter months: A comparison of observational data with the IRI descriptions. Adv. Space Res. 37(5), 1007-1017, https://doi.org/10.1016/j.asr.2005.06.074, 2006.

Abdu M.A., Souza J.R.D., Batista I.S., Sobral J.H.A. Equatorial spread F statistics and empirical representation for IRI: A regional model for the Brazilian longitude sector. Adv. Space Res. 31(3), 703-716, doi:10.1016/S0273-1177(03)00031-0, 2003.

P. Alken, E. Thébault, C. D. Beggan, H. Amit, J. Aubert, J. Baerenzung, T. N. Bondar, W. J. Brown, S. Califf, A. Chambodut, A. Chulliat, G. A. Cox, C. C. Finlay, A. Fournier, N. Gillet, A. Grayver, M. D. Hammer, M. Holschneider, L. Huder, G. Hulot, T. Jager, C. Kloss, M. Korte, W. Kuang, A. Kuvshinov, B. Langlais, J.-M. Léger, V. Lesur, P. W. Livermore, F. J. Lowes, S. Macmillan, W. Magnes, M. Mandea, S. Marsal, J. Matzka, M. C. Metman, T. Minami, A. Morschhauser, J. E. Mound, M. Nair, S. Nakano, N. Olsen, F. J. Pavón-Carrasco, V. G. Petrov, G. Ropp, M. Rother, T. J. Sabaka, S. Sanchez, D. Saturnino, N. R. Schnepf, X. Shen, C. Stolle, A. Tangborn, L. Tøffner-Clausen, H. Toh, J. M. Torta, J. Varner, F. Vervelidou, P. Vigneron, I. Wardinski, J. Wicht, A. Woods, Y. Yang, Z. Zeren and B. Zhou. International geomagnetic reference field: the thirteenth generation. Earth Planets Space 73, 1-25, https://doi.org/10.1186/s40623-020-01313-z, 2021.

Appleton E.V. Two anomalies in the ionosphere. Nature 157, 691, https://doi.org/10.1038/157691a0, 1946.

Bailey D.K. The geomagnetic nature of the F2-layer longitude-effect. Terr. Magn. Atmos. Electr. 53(1), 35-39, doi: 10.1029/TE053I001P00035, 1948.

Bhattacharyya A., Basu S., Groves K.M., Valladares C.E., Sheehan R. Dynamics of equatorial F region irregularities from spaced receiver scintillation observations. Geophys. Res. Lett. 28(1), https://doi.org/10.1029/2000GL012288, 119-122, 2001.

Briggs B.H., Phillips G.J., Shinn D.H. The analysis of observations on spaced receivers of the fading of radio signals. Proc. Phys. Soc. Sect. B 63(2), 106-121. https://doi.org/10.1088/0370-1301/63/2/305, 1950.

Carrano C.S. and Groves K.M. Temporal decorrelation of GPS satellite signals due to multiple scattering from ionospheric irregularities. In Proceedings of the 23rd International Technical Meeting of the Satellite Division of the Institute of Navigation (ION GNSS 2010) (pp. 361-374), 72010, September.

Cerruti A.P., Ledvina B.M., Kintner P.M. Scattering height estimation using scintillating wide area augmentation system/satellite based augmentation system and GPS satellite signals. Radio Sci. 41(06), 1-8, https://doi.org/10.1029/2005RS003405, 2006.

400   Cesaroni, C., Spogli, L., Franceschi, G.D., Damaceno, J.G., Grzesiak, M., Vani, B., Monico, J.F., Romano, V., Alfonsi, L., and Cafaro, M. A measure of ionospheric irregularities: Zonal velocity and its implications for L-band scintillation at low-latitudes. Earth Planet. Phys. 5(5), 450-461, https://doi.org/10.26464/epp2021042, 2021.

Chapagain N.P., Makela J.J., Meriwether J.W., Fisher D.J., Buriti R.A., Medeiros A.F. Comparison of nighttime zonal neutral
405   winds and equatorial plasma bubble drift velocities over Brazil. J. Geophys. Res. 117, A06309. doi:10.1029/2012JA017620, 2012.

Coley W.R., Heelis R.A., Spencer N.W. Comparison of low-latitude ion and neutral zonal drifts using DE 2 data. J. Geophys. Res. 99(A1), 341-348. https://doi.org/10.1029/93JA02205, 1994.
410

De Paula E.R., Muella M.T.A.H., Sobral J.H.A., Abdu M.A., Batista I.S., Beach T.L., Groves K.M. Magnetic conjugate point observations of kilometer and hundred-meter scale irregularities and zonal drifts. J. Geophys. Res. 115, A08307. doi:10.1029/2010JA015383, 2010.

415   Drob D.P., et al. An update to the Horizontal Wind Model (HWM): The quiet time thermosphere. Earth Space Sci. 2, 301-319. doi:10.1002/2014EA000089, 2015.

Dyson P.L., Benson R.F. Topside sounder observations of equatorial bubbles. Geophys. Res. Lett. 5(9), 795-798. doi:10.1029/GL005i009p00795, 1978.
420

Farley D.T., Bonelli E., Fejer B.G., Larsen M.F. The prereversal enhancement of the zonal electric field in the equatorial ionosphere. J. Geophys. Res. Space Phys. 91(A12), 13723-13728, https://doi.org/10.1029/JA091iA12p13723, 1986.

Fejer B.G., de Paula E.R., Gonzales S.A., Woodman R.F. Average vertical and zonal F-region plasma drifts over Jicamarca.
425   J. Geophys. Res. 96(A8), 13901-13906. doi:10.1029/91JA01171, 1991.

Fejer B.G., de Souza J., Santos A.S., Costa Pereira A.E. Climatology of F region zonal plasma drifts over Jicamarca. J. Geophys. Res. 110, A12310. doi:10.1029/2005JA011324, 2005.

430   Fejer B.G., Scherliess L., de Paula E.R. Effects of the vertical plasma drift velocity on the generation and evolution of equatorial spread F. J. Geophys. Res. Space Phys. 104(A9), 19859-19869, https://doi.org/10.1029/1999JA900271, 1999.

Fesen C.G., Crowley G., Roble R.G., Richmond A.D., Fejer B.G. Simulation of the pre-reversal enhancement in the low latitude vertical ion drifts. Geophys. Res. Lett. 27(13), 1851-1854, https://doi.org/10.1029/2000GL000061, 2000.

435

Gomez Socola J., Rodrigues F.S. ScintPi 2.0 and 3.0: low-cost GNSS-based monitors of ionospheric scintillation and total electron content. Earth Planets Space 74(1), 185 , https://doi.org/10.1186/s40623-022-01743-x, 2022.

Gomez Socola J., Sousasantos J., Rodrigues F.S., Brum C.G.M., Terra P., Moraes A.O., Eastes R. On the quiet-time occurrence

440   rates, severity and origin of L-band ionospheric scintillations observed from low-to-mid latitude sites located in Puerto Rico. J. Atmos. Sol.-Terr. Phys. 250, 106123, https://doi.org/10.1016/j.jastp.2023.106123, 2023.

Gomez Socola J. Data sets for ScintPi measurements of low-latitude ionospheric irregularity drifts using the spaced-receiver technique and SBAS signals [Dataset]. Zenodo https://zenodo.org/records/14289996, 2024.

445

Groves K.M., Basu S., Weber E.J., Smitham M., Kuenzler H., Valladares C.E., Sheehan R., Mackenzie E., Secan J.A., P. Ning, Mcneill W.J., Moonan D.W and Kendra M.J. Equatorial scintillation and systems support. Radio Sci. 32(5), 2047-2064, https://doi.org/10.1029/97RS00836, 1997.

450   Haerendel G.E., Eccles J.V., Çakir S. Theory of modeling the equatorial evening ionosphere and the origin of the shear in the horizontal plasma flow. J. Geophys. Res. 97(A2), 1209-1223. doi:10.1029/91JA02226, 1992.

Hanson W.B., Moffett R.J. Ionization transport effects in the equatorial F-region. J. Geophys. Res. 71(23), 5559-5572 , https://doi.org/10.1029/JZ071i023p05559, 1966.

455

Heelis R.A., Kendall P.C., Moffett R.J., Windle D.W., Rishbeth H. Electrical coupling of the E- and F-regions and its effect of F-region drifts and winds. Planet. Space Sci. 22, 743-756 , https://doi.org/10.1016/0032-0633(74)90144-5, 1974.

Immel T.J., Sagawa E., England S.L., Henderson S.B., Hagan M.E., Mende S.B., Frey H.U., Swenson C.M., Paxton L.J.

460   Control of equatorial ionospheric morphology by atmospheric tides. Geophys. Res. Lett. 33, L15108. doi:10.1029/2006GL026161, 2006.

Kil H., Kintner P.M., de Paula E.R., Kantor I.J. Latitudinal variations of scintillation activity and zonal plasma drifts in South America. Radio Sci. 37(1), 1-7, https://doi.org/10.1029/2001RS002468, 2002.

465

Kil H., Kintner P.M., de Paula E.R., Kantor I.J. Global Positioning System measurements of the ionospheric zonal apparent velocity at Cachoeira Paulista in Brazil. J. Geophys. Res. 105(A3), 5317-5327. doi:10.1029/1999JA000244 (2000).

Kintner P.M., Ledvina B.M. The ionosphere, radio navigation, and global navigation satellite systems. Adv. Space Res. 35(5), https://doi.org/10.1016/j.asr.2004.12.076, 2005.

Kintner P.M., Ledvina B.M., de Paula E.R., Kantor I.J. Size, shape, orientation, speed, and duration of GPS equatorial anomaly scintillations. Radio Sci. 39(2), 1-23, https://doi.org/10.1029/2003RS002878, 2004.

Ledvina B.M., Kintner P.M., de Paula E.R. Understanding spaced-receiver zonal velocity estimation. J. Geophys. Res. 109, A10306. doi:10.1029/2004JA, 2004.

Martinis, C., Hickey, D., Wroten, J., Baumgardner, J., Macinnis, R., Sullivan, C., & Padilla, S. All-Sky Imager Observations of the Latitudinal Extent and Zonal Motion of Magnetically Conjugate 630.0 nm Airglow Depletions. Atmosphere, 11, 642. doi:10.3390/atmos11060642, 2020.

Martinis, C., Eccles, J. V., Baumgardner, J., Manzano, J., & Mendillo, M. Latitude dependence of zonal plasma drifts obtained from dual-site airglow observations. J. Geophys. Res., 108, 1129. doi:10.1029/2002JA009462, 2003.

Mendillo, M., & Baumgardner, J. Airglow characteristics of equatorial plasma depletions. J. Geophys. Res. Space Phys., 87, 7641-7652, https://doi.org/10.1029/JA087iA09p07641, 1982.

Moffett, R. J. Equatorial anomaly in the electron distribution of the terrestrial F-region. Fundam. Cosmic Phys., 4, 1979.

Muella, M. T. A. H., de Paula, E. R., and Monteiro, A. A. Ionospheric Scintillation and Dynamics of Fresnel-Scale Irregularities in the Inner Region of the Equatorial Ionization Anomaly. Surv. Geophys., 34, 233–251. doi:10.1007/s10712-012-9212-0, 2013.

Muella, M. T. A. H., De Paula, E. R., Kantor, I. J., Rezende, L. F. C. D., & Smorigo, P. F. Occurrence and zonal drifts of small-scale ionospheric irregularities over an equatorial station during solar maximum–magnetic quiet and disturbed conditions. Adv. Space Res., 43, 1957-1973, 10.1016/j.asr.2009.03.017, 2009.

Muella, M. T. A. H., Duarte-Silva, M. H., Moraes, A. O., de Paula, E. R., de Rezende, L. F. C., Alfonsi, L., and Affonso, B. J. Climatology and modeling of ionospheric scintillations and irregularity zonal drifts at the equatorial anomaly crest region. Ann. Geophys., 35, 1201–1218. doi:10.5194/angeo-35-1201-2017, 2017.

500   Muella, M. T. D. A. H., De Paula, E. R., Kantor, I. J., Batista, I. S., Sobral, J. H. A., Abdu, M. A., Smorigo, P. F. GPS L-band scintillations and ionospheric irregularity zonal drifts inferred at equatorial and low-latitude regions. J. Atmos. Sol.-Terr. Phys., 70, 1261-1272, 10.1016/j.jastp.2008.03.013, 2008.

505   Muella, M.T.A.H., de Paula, E.R., & Jonah, O.F. GPS L1-Frequency Observations of Equatorial Scintillations and Irregularity Zonal Velocities. Surv. Geophys., 35, 335–357. doi:10.1007/s10712-013-9252-0, 2014.

Nava B, Radicella SM, Leitinger R, Coïsson P. Use of total electron content data to analyze ionosphere electron density gradients. Adv Space Res 39(8):1292–1297. doi:10.1016/j.asr.2007.01.041, 2007

510

Navarro, L. A., & Fejer, B.G. Storm-time coupling of equatorial nighttime F region neutral winds and plasma drifts. J. Geophys. Res. Space Phys., 125, e2020JA028253. doi:10.1029/2020JA028253, 2020.

Nishioka, M., Basu, S., Basu, S., Valladares, C. E., Sheehan, R. E., Roddy, P. A., & Groves, K. M. C/NOFS satellite
515   observations of equatorial ionospheric plasma structures supported by multiple ground-based diagnostics in October 2008. J. Geophys. Res. Space Phys., 116, A10. doi:10.1029/2011JA016446, 2011.

Otsuka, Y., Shiokawa, K., and Ogawa, T. Equatorial ionospheric scintillations and zonal irregularity drifts observed with closely-spaced GPS receivers in Indonesia. J. Atmos. Sol.-Terr. Phys., 84, 343-351, https://doi.org/10.2151/jmsj.84A.343,
520   2006.

Prol, F. S., Camargo, P. O., and Muella, M. T. A. H. Comparative Study Of Methods For Calculating Ionospheric Points And Describing The GNSS Signal Path. Bol. Ciênc. Geod., 23, 4, 10.1590/s1982-21702017000400044, 2017.

525   Rishbeth, H. Thermospheric winds and the F-region: A review. J. Atmos. Terr. Phys., 34, 1–47, https://doi.org/10.1016/0021-9169(72)90003-7, 1972.

Rodrigues, F. S., & Moraes, A. O. ScintPi: A low-cost, easy-to-build GPS ionospheric scintillation monitor for DASI studies of space weather, education, and citizen science initiatives. Earth Space Sci., 6, 1547-1560,
530   https://doi.org/10.1029/2019EA000588, 2019.

Shidler, S.A., Rodrigues, F.S. On a simple, data-aided analytic description of the morphology of equatorial F-region zonal plasma drifts. Prog Earth Planet Sci., 8, 26. doi:10.1186/s40645-021-00417-8, 2021.

535   Sobral, J. H. A., Abdu, M. A., Pedersen, T. R., Castilho, V. M., Arruda, D. C., Muella, M. T., ... & Bertoni, F. C. P. Ionospheric zonal velocities at conjugate points over Brazil during the COPEX campaign: Experimental observations and theoretical validations. J. Geophys. Res. Space Phys., 114, A4. doi:10.1029/2009JA014084, 2009.

540   Sousasantos J., Gomez Socola J., Rodrigues F.S., Eastes R.W., Brum C.G., Terra P. Severe L-band scintillation over low-to-mid latitudes caused by an extreme equatorial plasma bubble: joint observations from ground-based monitors and GOLD. Earth Planets Space 75(1), 41. https://doi.org/10.1186/s40623-023-01684-7 (2023).

Sousasantos J., Rodrigues F.S., Gomez Socola J., Pérez C., Colvero F., Martinis C.R., Wrasse C.M. First observations of severe scintillation over low-to-mid latitudes driven by quiet-time extreme equatorial plasma bubbles: Conjugate 545   measurements enabled by citizen science initiatives. J. Geophys. Res. Space Phys. 129, e2024JA032545. https://doi.org/10.1029/2024JA032545 (2024).

Spatz D.E., Franke S.J., Yeh K.C. Analysis and interpretation of spaced receiver scintillation data recorded at an equatorial station. Radio Sci. 23(3), 347-361. https://doi.org/10.1029/RS023i003p00347 (1988).

550

Valladares C.E., Meriwether J.W., Sheehan R., Biondi M.A. Correlative study of neutral winds and scintillation drifts measured near the magnetic equator. J. Geophys. Res. Space Phys. 107(A7), SIA-7. https://doi.org/10.1029/2001JA000042 (2002).

555   Wang W., Burns A.G., Liu J., Wang W., Zhang Y., Paxton L.J. (eds). Upper Thermospheric Winds. In Upper Atmosphere Dynamics and Energetics. https://doi.org/10.1002/9781119815631.ch3 (2021).

Wharton L.E., Spencer N.W., Mayr H.G. The Earth's thermospheric superrotation from Dynamics Explorer 2. Geophys. Res. Lett. 11(5), 531-533. https://doi.org/10.1029/GL011i005p00531 (1984).

560

Wright I.G., Rodrigues F.S., Gomez Socola J., Moraes A.O., Monico J.F.G., et al. On the detection of a solar radio burst event that occurred on 28 August 2022 and its effect on GNSS signals as observed by ionospheric scintillation monitors distributed over the American sector. J. Space Weather Space Clim. 13, 28. https://doi.org/10.1051/swsc/2023027, 2023a.

565   Wright I.G., Solanki I., Desai A., Socola J.G., Rodrigues F.S. Student-led design, development and tests of an autonomous, low-cost platform for distributed space weather observations. J. Space Weather Space Clim. 13, 12. https://doi.org/10.1051/swsc/2023001, 2023b.